







Performance characteristics of phase-change integrated silicon nitride photonic devices in the O and C telecommunications bands

JOAQUIN FANCA,^{1,2}  SANTIAGO GARCIA-CUEVAS CARRILLO,¹
EMANUELE GEMO,¹  CARLOTA RUIZ DE GALARRETA,¹ THALÍA
DOMÍNGUEZ BUCIO,²  FREDERIC Y. GARDES,²  HARISH
BHASKARAN,³  WOLFRAM H. P. PERNICE,⁴ C. DAVID
WRIGHT,^{1,*}  AND ANNA BALDYCHEVA¹

¹Department of Engineering, University of Exeter, Exeter, EX4 4QF, UK

²Optoelectronics Research Centre, University of Southampton, Southampton, SO17 1BJ, UK

³Department of Materials, University of Oxford, Parks Road, Oxford, OX1 3PH, UK

⁴Institute of Physics, University of Muenster, Heisenbergstr, 11, 48149 Muenster, Germany

*david.wright@exeter.ac.uk

Abstract: The evaluation and comparison of the optical properties in the O and C bands of silicon nitride rib waveguides with integrated Ge₂Sb₂Te₅ phase-change cells is reported. In straight rib waveguides, a high transmission contrast is observed in both bands when the Ge₂Sb₂Te₅ cell is switched between states, being up to 2.5 dB/μm in the C-band and 6.4 dB/μm in the O-band. In the case of silicon nitride ring resonator waveguides, high quality factor resonances ($Q \sim 10^5$) are found in both bands, leading to the provision of an ON-OFF switch characterized by an extinction ratio of 12 and 18 dB in O and C bands respectively. Finally, with the view to provide a comparison of the wavelength-dependent optical switching of the phase-change cell, a 3-dimensional finite-element method simulation is performed and a comparison of the optical-to-thermal energy conversion in both bands given.

Published by The Optical Society under the terms of the [Creative Commons Attribution 4.0 License](https://creativecommons.org/licenses/by/4.0/)

1. Introduction

To date, one of the challenges faced by silicon photonics is the integration of non-volatile reconfigurable components such as switches, filters, memories, though recently significant progress has been made, in particular by combining chalcogenide phase-change materials with photonic devices (see e.g. [1–4]).

Silicon nitride (SiN_x), an associated CMOS photonics enabling material, provides a very promising and complementary photonic platform for the development of low-cost CMOS compatible waveguides and related photonic components [5]. This is due to the flexibility of the material in terms of fabrication (low temperature), tuneability of the refractive index contrast, transparency, and low temperature sensitivity [6]. As a result, SiN_x waveguides have been widely employed for light propagation in the near infrared and in the visible range of the electromagnetic spectrum [7,8]. Although Si waveguides provide more confinement than SiN_x, leading to more compact devices, Si₃N₄ or non-stoichiometric SiN_x is more cost effective, thermally stable, and provides lower loss and greater freedom when constructing more complex multi-layer photonic circuitry [9,10].

Chalcogenide phase-change materials have been a mature technology for decades in optical storage and are now seen as a promising CMOS compatible route to provide the much needed non-volatile reconfigurability in integrated photonic components [11]. The phase-change materials (PCMs) [2,12,13] are stable (years at room temperature) in both amorphous or crystalline phases (which exhibit large contrast in optical properties), can be switched between states very

quickly (nanoseconds or less) [14,15], and exhibit high endurance (large number of switching cycles) [16,17]. The crucial feature of integrated photonic PCM-based devices compared with conventional thermo-optic based programmable circuits is that energy is only consumed during the actual switching process. Different technological applications of PCM-based devices such as switches [18,19], wavelength division multiplexers [20], directional couplers [21], memories [1,20,22,23] and neuron and synapse mimics [24,25] have been already demonstrated, all operating in the C-band range of the spectrum and using $\text{Ge}_2\text{Sb}_2\text{Te}_5$ phase-change cells. Recently, an O-band nitrogen rich silicon nitride Mach-Zehnder interferometer has been demonstrated in Ref. [26]. The contrast between the phase-change optical material properties (n and k) is used as the key component for phase-change photonic device operation and the values used for the films in this paper are as in Fig. 1, obtained by ellipsometric measurements. The optical constants for GST at 1310 and 1550 are $n_{1310}^{a\text{-GST}} = 3.969 + j0.23$ and $n_{1550}^{a\text{-GST}} = 3.94 + j0.045$ for the amorphous state, and $n_{1310}^{c\text{-GST}} = 6.15 + 1.57$ and $n_{1550}^{c\text{-GST}} = 6.11 + 0.83$ for the crystalline state.

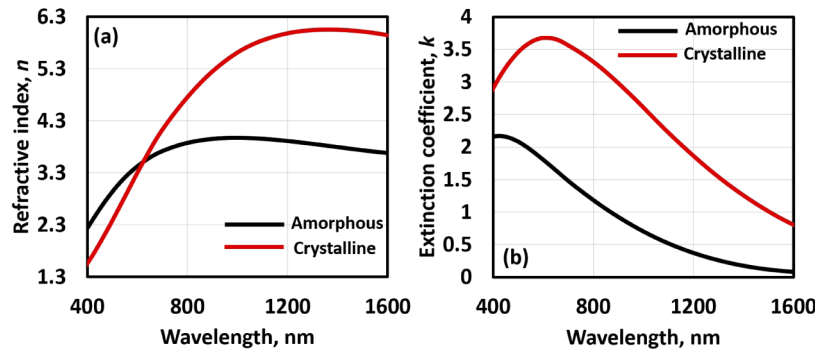


Fig. 1. (a) Refractive index, n , and (b) extinction coefficient, k , ellipsometry measurements in amorphous (solid black lines) and crystalline (solid red lines) state for $\text{Ge}_2\text{Sb}_2\text{Te}_5$ (GST).

Photonic integrated circuit applications are mainly conducted in the wavelength region where optical fibers have low transmission loss. This low-loss wavelength region ranges from 1260 nm to 1625 nm, and is divided into five wavelength bands referred to as the O-, E-, S-, C- and L-bands.

The O-band, ranging from 1260 nm to 1360 nm, stands for the original band. It was originally considered as the primary wavelength band used for optical communication in the mid-1970s for two main reasons: firstly, optical fibers at that time exhibited the lowest attenuation near the O-band, not in the C-band (due to water-based absorption in fibers available in the 1970s being in general less in the O band than in the C band - something that is no longer the case), and secondly, silica glass has a zero-material dispersion wavelength in the O-band, and thus it was expected that signal distortion, arising from fiber chromatic dispersion, would be minimized. Even though optical fiber manufacturing technology has improved and nearly achieved the elimination of water molecules, moving the lowest attenuation to the C-band, the O-band is still in extensive use for optical communication, mainly because optical communication systems that do not require dispersion-compensation schemes offer advantages in both the initial investment (lower transceiver price) and operation cost (lower power consumption), both key requirements for a data center where high-speed Ethernet is heavily used.

The C-band (conventional band: 1530-1565 nm) is commonly used in many metro, long-haul, ultra-long-haul optical transmission systems combined with wavelength-division multiplexing (WDM) and erbium-doped fiber amplifier (EDFA) technologies. The C-band is favored for long-distance transmission because the attenuation of modern optical fiber has its minimum in

the C-band, as discussed previously. The current lowest loss of optical fiber is 0.14 dB/km at 1560 nm, reported in 2018 [27,28].

In this manuscript, an experimental evaluation and comparison of the optical properties in the O and C bands of silicon nitride rib waveguides with integrated $\text{Ge}_2\text{Sb}_2\text{Te}_5$ phase-change cells is reported, with a view to possible future applications in both ranges of the spectrum. Furthermore, ring resonators with $\text{Ge}_2\text{Sb}_2\text{Te}_5$ (GST) deposited on top of the ring structure and used to turn ON or OFF the resonance are reported in both bands, demonstrating the building blocks for potential future application in opto-electronic oscillators (OEO) [29], frequency combs [30], multifunctional reconfigurable photonic integrated circuits (PICs) [31], or arbitrary radiofrequency waveform generators (AWG) [32].

2. Design

2.1. O-band

In the O-band, the optical platform consists of a Si_3N_4 ($n = 2.01$) rib photonic waveguide. The rib width and inner height are designated as $W = 900$ nm and $H = 300$ nm respectively, and the outer region of the rib has a thickness of $H - h = 120$ nm, see Figs. 2(a-b). This waveguide geometry enables mode propagation in the O-band (both TM and TE) with losses (< 1 dB/cm).

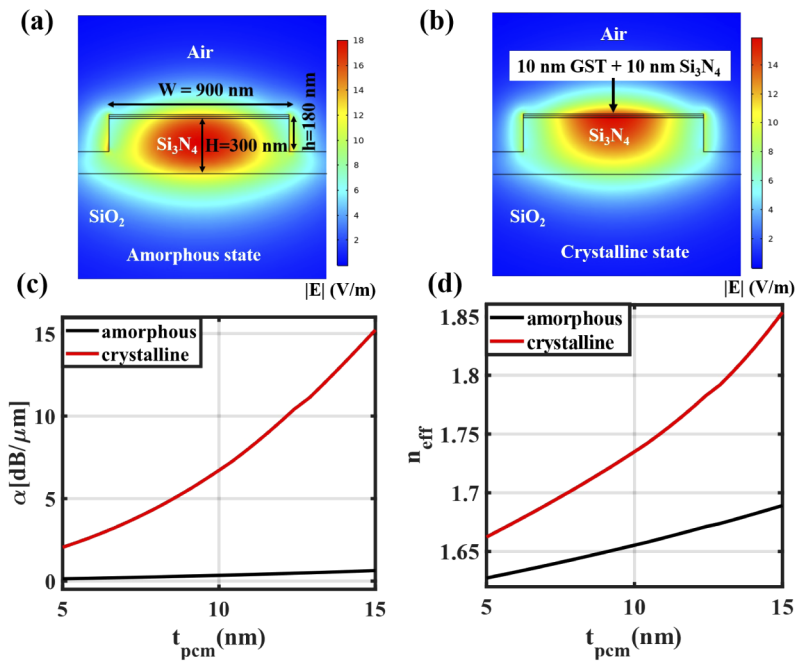


Fig. 2. Eigenmode simulation of the fundamental TE optical mode of a rib silicon nitride waveguide at 1310 nm wavelength, with a GST thin layer cell on top in the (a) amorphous state (b) crystalline state; (c) mode attenuation and (d) effective refractive index both as a function of PCM layer thickness.

TE polarization was selected in this work due to the grating couplers' fabrication optimization and the stronger mode overlap compared with the TM mode. A phase-change material cell was deposited on top of the rib waveguide in order to make the passive building block tunable. The tunability consists of controlling the losses of the waveguide by switching the PCM layer between its amorphous and crystalline states. The thickness of the cells was selected to be 20 nm, comprising a 10 nm PCM ($\text{Ge}_2\text{Sb}_2\text{Te}_5$) layer, capped with 10 nm of Si_3N_4 to prevent

oxidation. In order to achieve a good contrast (distinguishable difference in attenuation between the amorphous and crystalline states of the phase change material cell) while at the same time maintaining a good signal-to-noise ratio in the output optical signal of the waveguide, a 10 nm thick PCM layer was selected for the devices which, as can be seen in Fig. 2(c-d), provides a good trade-off between contrast and output signal level. COMSOL Multiphysics was used to calculate the effective refractive indices and the cell absorption in both states of the PCM (amorphous and crystalline), see Figs. 2(a-b). The attenuation constant (α) and the effective refractive index (n_{eff}) of the structure strongly depend on the thickness of the PCM layer (t_{pcm}) as shown in Figs. 2(c-d). The optical constants used in the simulations at 1310 nm can be found in Fig. 1.

2.2. C-band

In the C-band, the optical platform consists of a Si_3N_4 ($n = 2.01$) rib photonic waveguide.

The rib width and inner height are designated as $W = 1300$ nm and $H = 300$ nm respectively, and the outer region of the rib has a thickness of $H - h = 120$ nm, see Figs. 3(a-b). This waveguide geometry enables mode propagation in the C-band (both TM and TE) with losses (< 1 dB/cm). The phase-change cell deposited on top of the waveguide is identical to that described above for the O-band, and COMSOL Multiphysics was again used to calculate the effective refractive indices and the cell absorption in both states of the PCM (amorphous and crystalline). As in the O-band, the absorption (attenuation) and the phase shift (effective index) induced by the phase change material strongly depend on the thickness of the PCM layer (t_{pcm}), as shown in Figs. 3(c-d). The optical constants used in the simulations at 1550 nm can be found in Fig. 1.

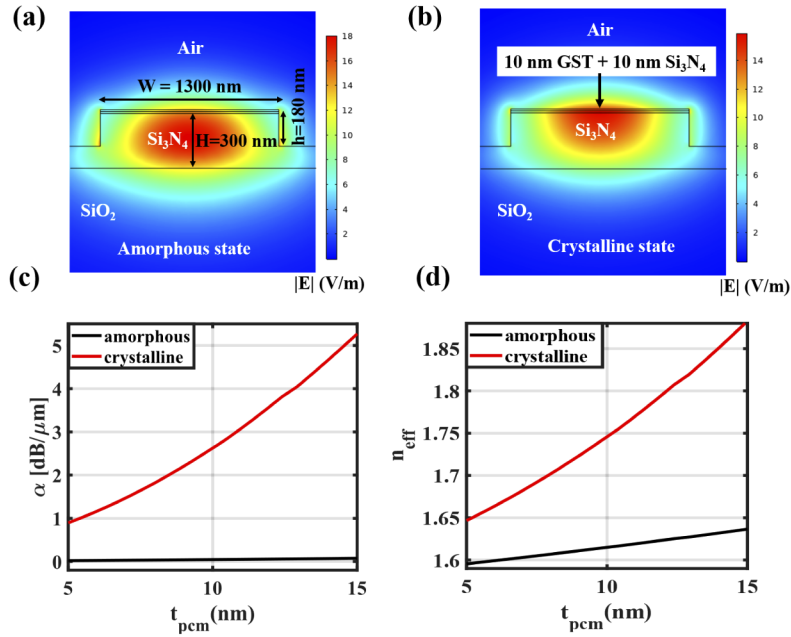


Fig. 3. Eigenmode simulation of the fundamental TE optical mode of a rib silicon nitride waveguide at 1550 nm wavelength, with a GST thin layer cell on top in the (a) amorphous state (b) crystalline state; (c) mode attenuation and (d) effective refractive index both as a function of PCM layer thickness.

3. Fabrication

The various devices were fabricated using electron beam lithography (EBL), using three exposure steps, on silicon nitride-on-insulator substrates. The layer stack consists of 300 nm of Si_3N_4 over $2\text{ }\mu\text{m}$ of SiO_2 , deposited on a silicon carrier wafer.

In a first lithography step, windows for gold alignment markers were opened using the PMMA 950K A4 resist spun at 4000 rpm for 60 seconds, yielding a resist film thickness of 200 nm. The development was carried out in an IPA: MIBK: MEK (15:5:1) mixture for 35 seconds. After depositing 5 nm of chromium and 50 nm of gold using a thermal evaporator (HHV Auto306), a lift-off in acetone was carried out and alignment marks for the next lithography steps were thus patterned. In a second lithography step, the waveguides and ring resonators were exposed using a TI PRIME adhesion promoter spun at 4000 rpm for 30 seconds and baked at 120°C for 120 seconds, and ma-N 2403 negative tone resist spun at 3500 rpm for 60 seconds and baked at 90°C for 120 seconds. The lift-off in this case was carried out using MF 319 developer for 35 seconds. This was followed by reactive ion etching (RIE) using a recipe which comprises a gas mixture of 15 standard cubic centimeters per minute (sccm) of SF_6 and 15 sccm of Argon with a pressure of 45 mTorr, and a power of 50 W, to pattern the photonic integrated waveguides and ring resonators on Si_3N_4 . The remaining resist was removed in an acetone bath at 80°C for 10 minutes, followed by 10 minutes of sonication in the warm acetone at 80 kHz. A third and last lithography step consisted of opening the windows for the PCM deposition using the same technique as used for the markers. Finally, the GST cells capped by 10 nm of Si_3N_4 were then integrated on top of the waveguides and rings using physical vapor deposition (PVD) techniques (magnetron sputtering). Examples of as-fabricated devices are shown in Fig. 4.

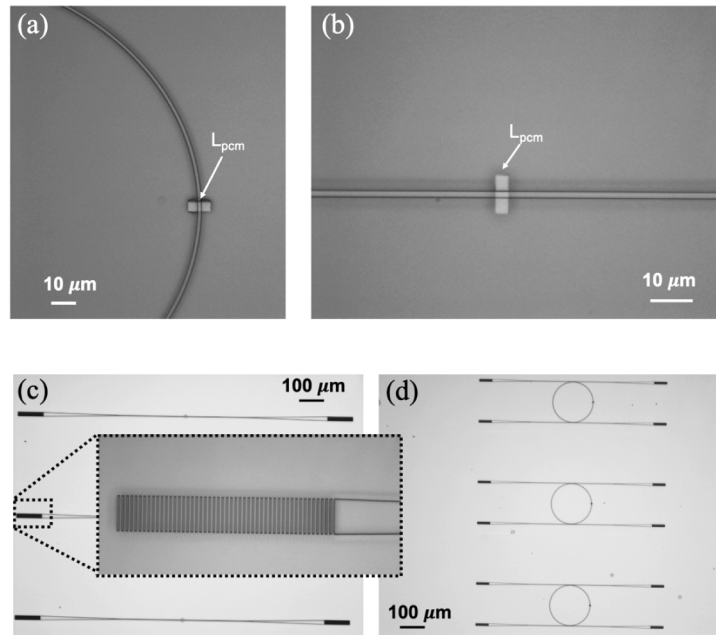


Fig. 4. Optical microscope images of the fabricated structures. (a) Rib micro-ring resonator waveguide at 1550 nm with the deposited phase change material GST. (b) Rib waveguide with a deposited GST cell with length $L_{pcm} = 4\text{ }\mu\text{m}$. (c) Rib waveguides with different lengths of the phase change material and a TE grating coupler inset image. (d) Add-drop filters with the phase change material deposited in the right-hand side of the ring resonator.

4. Results and discussion

4.1. O-band

A set of rib waveguides and ring resonators with width and inner height values of $W = 900$ nm and $H = 300$ nm respectively, and the outer region of the rib waveguide with a thickness of 120 nm were fabricated in the O-band. The radii of the ring resonators were selected to be large enough in order to avoid bending losses and obtain high quality factor resonances ($Q \sim 10^5$) without the phase change material cell. All structures were connected to an input and an output grating coupler which consists of a $10\ \mu\text{m}$ width and $50\ \mu\text{m}$ length with a period of 984 nm tapered down to a single-mode waveguide of 900 nm width. The angle between the optical fibers delivering light to the couplers and the couplers themselves was selected to be 14° to the normal, to ensure maximum coupling at the wavelength of interest (1310 nm). The spectral response of the rib waveguide integrated structures for different PCM cell lengths, ranging from $1\ \mu\text{m}$ up to $25\ \mu\text{m}$, and for both amorphous and crystalline states of the PCM layer, was evaluated using an Agilent 8164B tunable laser source with a tunable wavelength of 1260 to 1360 nm. The polarization of the light was controlled to ensure that only TE modes could propagate through the devices. The measurements of the different rib waveguides for different cell lengths were normalized, extracting the losses due to the grating couplers. The phase change was induced thermally by depositing the chip on a hot plate at 230°C for 15 min. The experimental losses of the waveguide at 1310 nm using GST as the deposited PCM were found to be as high as $6.66\ \text{dB}/\mu\text{m}$ in the crystalline state and as low as $0.228\ \text{dB}/\mu\text{m}$ in the amorphous state [Fig. 5(a)]. These results matched quite closely the simulated values, which at 1310 are $6.71\ \text{dB}/\mu\text{m}$ and $0.34\ \text{dB}/\mu\text{m}$ in the crystalline and amorphous states respectively [Fig. 2(c)]. The loss coefficient of the TE mode for both states of the phase change material was also evaluated experimentally over a range of the spectrum between 1260 and 1360 nm, with losses in the crystalline state showing a slight increase with wavelength, whereas losses in the amorphous state being almost flat, as shown in Fig. 5(b). For the O-band a scattering loss of 0.22 dB in the amorphous state and 0.33 dB in the crystalline state have been evaluated.

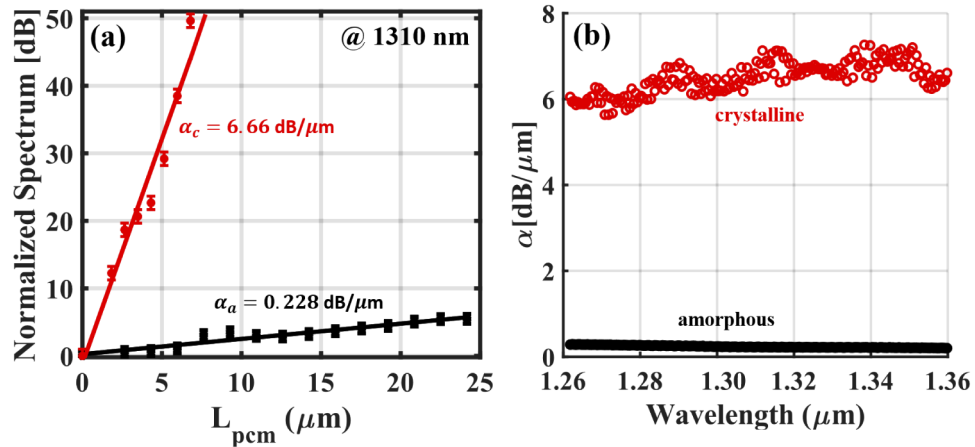


Fig. 5. (a) Measured losses in the waveguide for different PCM cell lengths in both states, amorphous (black line) and crystalline (red line) at 1310 nm. (b) Measured loss coefficient for different wavelengths in both cell states, amorphous (black dots) and crystalline (red dots).

A set of 5 rib ring resonator waveguides, each with their own integrated PCM cell, were also coupled to straight waveguides in order to measure their non-volatile tunable resonance properties

in the O-band. The rib ring resonators were designed to have radii of $100\ \mu\text{m}$ in order to avoid bending losses. The gap between the ring resonator and the straight waveguide was set to be around $250\ \text{nm}$. A GST cell of $5\ \mu\text{m}$ length and width of $8\ \mu\text{m}$ completely covering the waveguide width was deposited on top of the ring resonator structure [Fig. 4(a)]. First, the bare structure (without phase change material) was characterized and normalized. The optical response can be seen (black dashed lines) in Fig. 6(a), and quality factors as large as $Q = 21,840$ were measured with a free-spectral range (FSR) of $1.4\ \text{nm}$. Using the resonance equation of a ring resonator, $m\lambda_m = 2\pi n_{\text{eff}} R$, the experimental effective refractive index can be extracted, where λ_m is the resonance wavelength, R is the radius of the ring resonator, m is the number of integer number of wavelengths inside the cavity and n_{eff} is the effective refractive index. In our case, $R = 100\ \mu\text{m}$, $m = 757$, and $\lambda_m = 1.31045\ \mu\text{m}$, hence, the measured effective refractive index has a value of $n_{\text{eff}} = 1.5948$, which agrees with the simulated extracted effective refractive index $n_{\text{eff}} = 1.5953$. In Fig. 6(a), the optical responses of the ring resonator structure for both states of the phase change material, amorphous (solid black line) and crystalline (solid red line) are also presented. In Fig. 6(b), a zoomed image of the resonance around $1310\ \text{nm}$ is presented. It can be seen that once the phase change material is switched to the crystalline state, the resonance condition is effectively cancelled (i.e. much more attenuated), due to the high extinction coefficient in the crystalline state, and we can consider the device to be in an OFF- state. However, when the phase change material is in the amorphous state, the ring resonator essentially maintains the original resonances, but shifted in wavelength, and we can consider this as the ON-state. The free spectral range (FSR) in the amorphous and crystalline states of the PCM is maintained and is equal to $1.4\ \text{nm}$ for both states. The quality factor is reduced for both states of the PCM as compared with the bare structure. For the amorphous state, the quality factor is however still relatively large, being $Q = 6590$, due to the low level of losses introduced by the amorphous phase. In the crystalline state, however, the quality factor goes down to $Q = 1450$. The wavelength shift of the resonance peaks compared with the bare structure resonances are $\Delta\lambda_a = 0.46\ \text{nm}$ and $\Delta\lambda_c = 0.63\ \text{nm}$ for amorphous and crystalline states respectively. The extinction ratio (ER) of the resonances in the amorphous state is as high as $12\ \text{dB}$ and in the crystalline state it goes down to $3\ \text{dB}$. In Fig. 6(b) an optical switch is shown at $1.3095\ \text{nm}$ where a difference in transmission between ON-OFF state of $10\ \text{dB}$ is produced.

In order to experimentally evaluate the effective refractive index of the PCM ring resonator structures, in amorphous and crystalline states of the phase change material cell, the following formula should be considered [33,34]:

$$\Delta n_{\text{eff}}^{(a-c)} = \frac{\lambda}{\text{FSR}} \cdot \frac{\Delta\lambda_{(a-c)}}{L_{\text{pcm}}} \quad (1)$$

where $\Delta n_{\text{eff}}^{(a-c)}$ is the variation produced in the effective refractive index when the PCM cell is introduced compared to the bare structure (no PCM), the superscripts a and c refer to the amorphous and crystalline states respectively, FSR is the free spectral range, L_{pcm} is the phase change material cell length, and $\Delta\lambda_{(a-c)}$ is the shift in the resonance peaks of the amorphous and crystalline states respect to the resonances produced by the bare ring resonator waveguide as introduced previously. The effective index, n_{eff} , is used instead of group index, n_g , because only a small portion of the ring resonator is modified by the inclusion of the PCM cell [34]. The variation in the effective refractive index due to the deposition of the phase change material is $\Delta n_{\text{eff}}^a = 0.0861$ and $\Delta n_{\text{eff}}^c = 0.1179$ for the amorphous and crystalline states respectively. Finally, the experimental effective refractive index of the PCM ring resonator structures can be evaluated, yielding to values of $n_{\text{eff}}^a = 1.68$ and $n_{\text{eff}}^c = 1.71$ for the amorphous and crystalline states respectively. These values are close to the simulated results for the effective refractive index, which were $n_{\text{eff}}^a = 1.66$ and $n_{\text{eff}}^c = 1.73$ [Fig. 2(d)] for the amorphous and crystalline states respectively, assuming a PCM layer thickness of $10\ \text{nm}$.

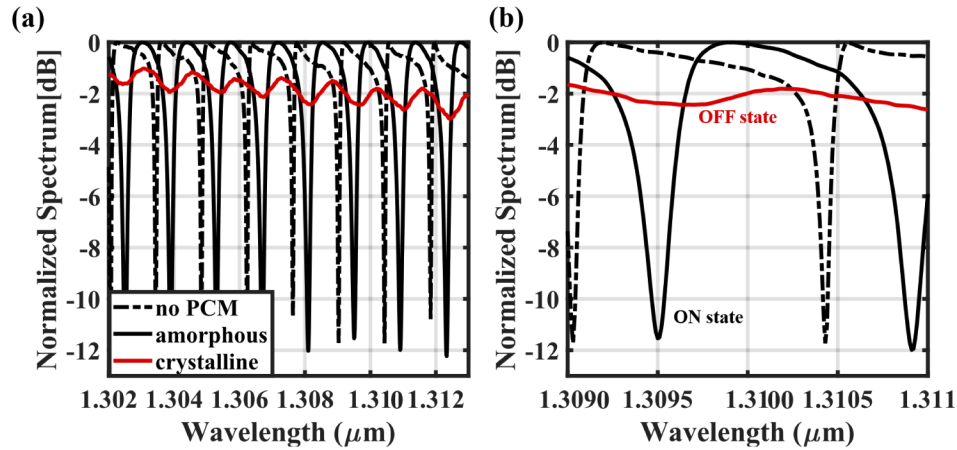


Fig. 6. (a) Normalized spectrum of a rib ring silicon nitride resonator waveguide with radius, $R = 100 \mu\text{m}$, for the bare structure, without the PCM (dashed black lines) and with a phase change material cell length, $L_{\text{pcm}} = 5 \mu\text{m}$ and $8 \mu\text{m}$ width deposited on top of the ring structure for both, the amorphous state of the PCM (solid black lines) and the crystalline state of the PCM (solid red line). (b) Zoom in image of the resonances in both states of the phase change material showing the device principle, ON-OFF operation.

4.2. C-band

For operation in the C-band, a set of rib waveguides and ring resonators with width and inner height values of $W = 1300 \text{ nm}$ and $H = 300 \text{ nm}$ respectively, and the outer region of the rib waveguide with a thickness of 120 nm were fabricated. Similar input/output couplers were used as described above, but in this case the grating period was 1195 nm and the couplers were tapered down in width to a single-mode waveguide of 1300 nm . As before, the spectral response of the rib waveguides was measured for PCM cell lengths from $1 \mu\text{m}$ to $25 \mu\text{m}$, for both amorphous and crystalline states of the phase change material. The experimental losses of the PCM waveguide at 1550 nm using GST as the deposited PCM were found to be as high as $2.86 \text{ dB}/\mu\text{m}$ in the crystalline state, and as low as $0.039 \text{ dB}/\mu\text{m}$ in the amorphous state [Fig. 7(a)]. These are again close to the simulated values for the losses at 1550 nm , which were $2.625 \text{ dB}/\mu\text{m}$ and $0.044 \text{ dB}/\mu\text{m}$ in the crystalline and amorphous states respectively [Fig. 3(c)]. These values are consistent with the recently published values in Ref. [35], and other previous work [36]. The experimentally loss coefficient of the TE mode for both states of the phase change material over a range of the spectrum between 1520 to 1610 nm is shown in Fig. 7(b), from where it can be seen that losses are essentially flat over this wavelength range. The scattering loss at 1550 nm is 0.45 dB in the crystalline state and 0.15 dB in the amorphous state.

The resonance properties of a set of 5 rib ring resonator waveguides designed for operation in the C-band were also experimentally evaluated, using the same procedures as described above for the O-band case. Here, a gap between the ring resonator and the waveguide was set to be around 300 nm , and a GST cell of $4 \mu\text{m}$ length and width of $8 \mu\text{m}$ completely covering the waveguide width was deposited on top of the ring resonator structure [Fig. 4(d)]. Results are shown in Fig. 8. Without any PCM layer, quality factors as large as $Q = 1.4 \cdot 10^4$ were measured, with a FSR of 2.02 nm . Using the resonance equation of a ring resonator described previously ($m\lambda_m = 2\pi n_{\text{eff}}R$), in this case with $R = 100 \mu\text{m}$, $m = 636$, and $\lambda_m = 1.5493$, the measured effective refractive index was found to be, $n_{\text{eff}} = 1.5682$, which agrees well with the simulated extracted effective refractive index $n_{\text{eff}} = 1.5688$. As in the case for O-band operation, once the PCM layer in the resonator structure is switched to the crystalline state, the resonance condition is effectively cancelled, but

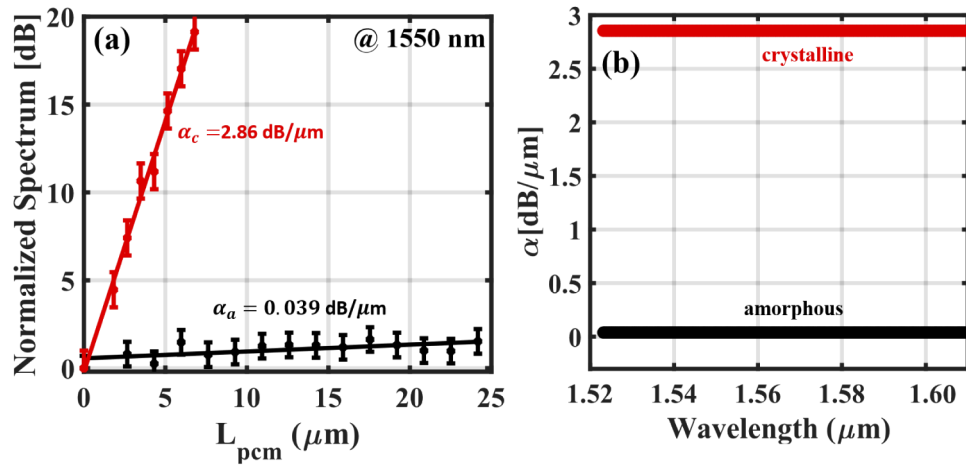


Fig. 7. (a) Measured losses in the waveguide for different PCM cell lengths in both states, amorphous (black line) and crystalline (red line) at 1550 nm. (b) Measured loss coefficient for different wavelengths in both cell states, amorphous (black dots) and crystalline (red dots).

with the PCM layer in the the amorphous state the ring resonator essentially maintains the original resonances, but slightly wavelength shifted (see Fig. 8(a) and zoomed version in Fig. 8(b)). The FSR in the amorphous and crystalline states of the PCM is maintained, and is equal to 2.02 nm for both states. The quality factor (Q) is again reduced for both states of the PCM as compared with the bare structure, being $Q = 3869$ for the amorphous state and $Q = 1938$ for the crystalline state. The distance between peaks compared with the bare structure resonances are $\Delta\lambda_a = 0.2 \text{ nm}$ and $\Delta\lambda_c = 1 \text{ nm}$ for amorphous and crystalline states respectively. The extinction ratio (ER) of the resonances in amorphous state are as high as 24 dB and in the crystalline state it goes down to 2 dB. In Fig. 8(b) an optical switch is shown at 1,5495 nm where a difference in transmission between ON-OFF state of 18 dB is produced. The variation in the effective refractive index due to the deposition of the phase change material is $\Delta n_{\text{eff}}^a = 0.0328$ and $\Delta n_{\text{eff}}^c = 0.1638$ for the amorphous and crystalline states respectively. Finally, the experimental effective refractive index of the PCM ring resonator structures can be evaluated, yielding to values of $n_{\text{eff}}^a = 1.60$ and $n_{\text{eff}}^c = 1.74$ for the amorphous and crystalline states respectively, again very close to the simulated values of $n_{\text{eff}}^a = 1.62$ and $n_{\text{eff}}^c = 1.75$ [Fig. 3(d)].

4.3. Comparison between O and C-bands

A complete performance comparison between the devices fabricated in the O and C-bands is presented in Table 1. In the O-band, the absorption is much higher than in the C-band for both states of the PCM, which implies that lower power energies will be required to switch the phase change material optically using laser pulses on-chip. However, the contrast in the effective refractive index is higher in the C-band. Consequently, if we operate in the O-band we might expect to be able to fabricate a complete set of low power consumption, nonvolatile photonic integrated circuits exploiting the large absorption contrast (between crystalline and amorphous states) in this spectral range. However, the readout signal amplitude (and hence the signal-to-noise-ratio) will also be reduced for a given readout signal power, as compared to the C-band. A large contrast between states can also make re-writability more difficult, as explained in Ref. [1], though this difficulty is alleviated somewhat by the use of the so-called double-step pulse for re-writing (see Ref. [37]). If the desired characteristic is a tuning in the optical phase

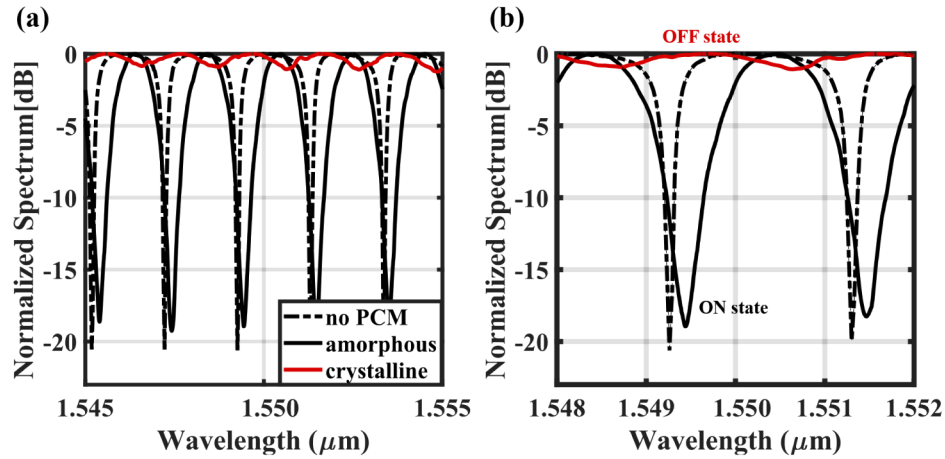


Fig. 8. (a) Normalized spectrum of a rib ring silicon nitride resonator waveguide with radius, $R = 100 \mu\text{m}$, for the bare structure, without the PCM (dashed black lines) and with a phase change material cell length, $L_{\text{pcm}} = 4 \mu\text{m}$ and $8 \mu\text{m}$ width deposited on top of the ring structure for both, the amorphous state of the PCM (solid black lines) and the crystalline state of the PCM (solid red line). (b) Zoom in image of the resonances in both states of the phase change material showing the device principle, ON-OFF operation.

without having large absorption, the C-band is no doubt a better selection than O-band, and of course many devices operating in the C-band and exploiting absorption contrast have already been demonstrated [38–41]. Thus, it is clear that operating in the O- and C-bands comes with various advantages and disadvantages, and that different building blocks for future emerging applications can be fabricated in both ranges of the spectrum. In this work we are concerned with amplitude modulation, but there are different applications in which optical phase modulation is required. In such cases, a useful figure-of-merit (FOM) is $\Delta n_{\text{eff}}^{a-c} / \Delta \alpha_{a-c}$ which, for the cases examined here, is approximately five times higher in the C-band as compared to the O-band ($\text{FOM}_{1310} = 0.01$, $\text{FOM}_{1550} = 0.05$).

Table 1. The device performance comparison between the O-band (1310 nm), C-band (1550 nm) and theoretical simulated results is presented.

Device performance	@1310 (Experimental)	@1310 (Simulated)	@1550 (Experimental)	@1550 (Simulated)
α_c	6.66 dB/ μm	6.71 dB/ μm	2.86 dB/ μm	2.63 dB/ μm
α_a	0.228 dB/ μm	0.34 dB/ μm	0.039 dB/ μm	0.044 dB/ μm
FSR	1.4 nm	1.7 nm	2 nm	2.4 nm
Q_a	6590	$6.4 \cdot 10^3$	3869	$3.7 \cdot 10^3$
Q_c	1450	$1.3 \cdot 10^3$	1938	$1.85 \cdot 10^3$
Q_{bare}	$2.2 \cdot 10^4$	$2 \cdot 10^4$	$1.4 \cdot 10^4$	$1 \cdot 10^4$
n_{eff}	1.5948	1.5953	1.5687	1.569
n_{eff}^a	1.68	1.66	1.60	1.62
n_{eff}^c	1.71	1.73	1.74	1.75
$\Delta \lambda_a$	0.46 nm	0.42 nm	0.2 nm	0.31 nm
$\Delta \lambda_c$	0.63 nm	0.85 nm	1 nm	1.1 nm
ER	12 dB	14 dB	18 dB	20 dB

With the view to provide a comparison of the wavelength-dependent optical switching performance, we performed a 3-dimensional FEM simulation of the O-band and C-band straight waveguide device with the PCM cell deposited on top, to observe the temperature profile arising from the delivery of a 15 mW, 20 ns rectangular pulse through the waveguide (as used for successful experimental switching at 1550 nm in Ref. [1]). Details of the modelling methodology may be found in Ref. [23]. We note that the thermo-optical effect is also a fundamental contribution to the time-dependent evolution of the PCM temperature profile, and so we include this effect in our model using data provided by Stegmaier et al. [42]. The simulation results are shown in Fig. 9, where it can be seen that when the PCM layer is in the crystalline phase the 15 mW, 20 ns switching pulse raises the peak temperature in the PCM layer above the melting temperature of GST (approximately 900 K) in both the O- and C-bands (Fig. 9(a)). When the PCM layer is amorphous, the same switching pulse raises the peak temperature to over 600 K in the O-band (a temperature conducive to rapid crystallization [43]), but in the C-band only a marginal increase in temperature, insufficient for crystallization, is observed. If we now turn to the average temperature in the PCM layer, as shown in Fig. 9(b), we observe that in the O-band the melting temperature (for a crystalline PCM layer) is reached after only 9 ns, whereas in the C-band the average temperature never reaches melting, again revealing a superior efficiency in the optical-to-thermal energy conversion in the former case.

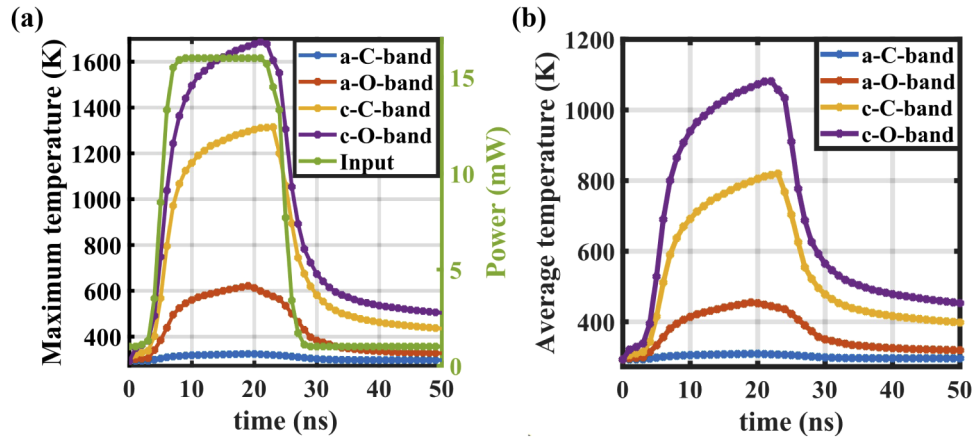


Fig. 9. (a) Maximum temperature and (b) average temperature reached in the PCM unit cell for four different states: amorphous state in the C-band (a-C-band) in blue, crystalline state in the C-band (c-C-band) in yellow, amorphous state in the O-band (a-O-band) in red and crystalline state in the O-band (c-O-band) in purple. Also, the input pulse is represented in the right axes of figure (a) in green.

As for the simulated recrystallization process (i.e. pulse delivery to the amorphous unit cell), in the C-band our simulation barely report any temperature increase. Instead, in the O-band we calculate a peak temperature of 600 K, and an average temperature of 450 K. Once more, the numerical results show how the higher optical loss in the O-band is responsible for a much more efficient temperature increase.

Following the approach proposed in Zheng et al. [44], we also report the energy efficiency η , of the straight waveguide devices, calculated as:

$$\eta = \frac{E_{GST}}{E_{pulse}} = \frac{\int \rho C_p (T - T_0) dV}{P_0 \Delta t}, \quad (2)$$

where ρ is the material density, C_p is the specific heat, T_0 is the initial ambient temperature (293 K), and the integral domain is over the entire GST film, P_0 is the pulse power and Δt is

the pulse width. With respect to the different wavelengths, we observe that the variation of η is marginal for the crystal case, with an efficiency value in the C-band slightly higher than the O-band, yielding a ratio between efficiencies (η_{1310}/η_{1550}) of 0.8. However, for the amorphous case, the O-band efficiency is typically around 4 times higher than the corresponding C-band value, in the whole range of investigated pulse duration.

5. Conclusions

In this manuscript a comparison between the O- and C-band optical properties of silicon nitride integrated photonic devices incorporating cells of the well-known phase change material, $\text{Ge}_2\text{Sb}_2\text{Te}_5$ has been given. For straight, rib type waveguides, a strong contrast in attenuation between amorphous and crystalline states of the PCM cell as high as $2.5 \text{ dB}/\mu\text{m}$ was observed in the C-band, and $6.4 \text{ dB}/\mu\text{m}$ in the O-band. High quality factor resonances were also observed in both bands for ring resonator devices, and an ON-OFF switch has been demonstrated in the O and C-bands with an ER of 12 and 18 dB respectively. A superior efficiency in terms of optical-to-thermal energy conversion (when sending optical pulses along the waveguide) in the O-band case was noted, as compared with the C-band, and this may be beneficial in terms of reducing the power consumed during switching of the PCM layer. This study thus provides useful characterization information for the operation of non-volatile integrated photonic circuits based on phase change materials in two of the most important spectral ranges used for optical communications, opening up the route to future potential applications in areas such as future application in opto-electronic oscillators, switches, memories, frequency combs, multifunctional reconfigurable photonic integrated circuits, arbitrary radiofrequency waveform generators etc.

Funding

Horizon 2020 Framework Programme (780848); Engineering and Physical Sciences Research Council (EP/L015331/1, EP/N013247/1, EP/R003076/1).

Disclosures

The authors declare no conflicts of interest.

Data Availability

Data relating to this manuscript can be obtained from the authors.

References

1. C. Ríos, M. Stegmaier, P. Hosseini, D. Wang, T. Scherer, C. D. Wright, H. Bhaskaran, and W. H. Pernice, "Integrated all-photonic non-volatile multi-level memory," *Nat. Photonics* **9**(11), 725–732 (2015).
2. M. Wuttig, H. Bhaskaran, and T. Taubner, "Phase-change materials for non-volatile photonic applications," *Nat. Photonics* **11**(8), 465–476 (2017).
3. C. D. Wright, H. Bhaskaran, and W. H. Pernice, "Integrated phase-change photonic devices and systems," *MRS Bull.* **44**(09), 721–727 (2019).
4. K. J. Miller, R. F. Haglund, and S. M. Weiss, "Optical phase change materials in integrated silicon photonic devices," *Opt. Mater. Express* **8**(8), 2415–2429 (2018).
5. T. Domínguez Bucio, C. Lacava, M. Clementi, J. Faneca, I. Skandalos, A. Baldycheva, M. Galli, K. Debnath, P. Petropoulos, and F. Gardes, "Silicon nitride photonics for the near-infrared," *IEEE J. Sel. Top. Quantum Electron.* **26**(2), 1–13 (2020).
6. T. Domínguez Bucio, A. Z. Khokhar, G. Z. Mashanovich, and F. Y. Gardes, "N-rich silicon nitride angled MMI for coarse wavelength division (de) multiplexing in the O-band," *Opt. Lett.* **43**(6), 1251–1254 (2018).
7. J. Milgram, J. Wojcik, P. Mascher, and A. Knights, "Optically pumped si nanocrystal emitter integrated with low loss silicon nitride waveguides," *Opt. Express* **15**(22), 14679–14688 (2007).
8. S. Gaugiran, S. Gétin, J.-M. Fedeli, G. Colas, A. Fuchs, F. Chatelain, and J. Dérourard, "Optical manipulation of microparticles and cells on silicon nitride waveguides," *Opt. Express* **13**(18), 6956–6963 (2005).

9. T. Domínguez Bucio, A. Z. Khokhar, C. Lacava, S. Stankovic, G. Z. Mashanovich, P. Petropoulos, and F. Y. Gardes, "Material and optical properties of low-temperature NH_3 -free PECVD SiN_x layers for photonic applications," *J. Phys. D: Appl. Phys.* **50**(2), 025106 (2017).
10. R. Baets, A. Z. Subramanian, S. Clemmen, B. Kuyken, P. Bienstman, N. Le Thomas, G. Roelkens, D. Van Thourhout, P. Helin, and S. Severi, "Silicon photonics: silicon nitride versus silicon-on-insulator," in *Optical Fiber Communication Conference* (Optical Society of America, 2016), pp. Th3J–1.
11. C. Ríos, M. Stegmaier, Z. Cheng, N. Youngblood, C. D. Wright, W. H. Pernice, and H. Bhaskaran, "Controlled switching of phase-change materials by evanescent-field coupling in integrated photonics," *Opt. Mater. Express* **8**(9), 2455–2470 (2018).
12. M. Wuttig and N. Yamada, "Phase-change materials for rewriteable data storage," *Nat. Mater.* **6**(11), 824–832 (2007).
13. R. Soref, "Tutorial: Integrated-photonics switching structures," *APL Photonics* **3**(2), 021101 (2018).
14. G. Bruns, P. Merkelbach, C. Schlockermann, M. Salinga, M. Wuttig, T. Happ, J. Philipp, and M. Kund, "Nanosecond switching in GeTe phase change memory cells," *Appl. Phys. Lett.* **95**(4), 043108 (2009).
15. N. Ciochini, M. Laudato, M. Boniardi, E. Varesi, P. Fantini, A. L. Lacaita, and D. Ielmini, "Bipolar switching in chalcogenide phase change memory," *Sci. Rep.* **6**(1), 29162 (2016).
16. P. Li, X. Yang, T. W. Maß, J. Hanss, M. Lewin, A.-K. U. Michel, M. Wuttig, and T. Taubner, "Reversible optical switching of highly confined phonon–polaritons with an ultrathin phase-change material," *Nat. Mater.* **15**(8), 870–875 (2016).
17. H. Y. Cheng, T. H. Hsu, S. Raoux, J. Y. Wu, P. Y. Du, M. Breitwisch, Y. Zhu, E. K. Lai, E. Joseph, S. Mittal, R. Cheek, A. Schrott, S. C. Lai, H. L. Lung, and C. Lam, "A high performance phase change memory with fast switching speed and high temperature retention by engineering the gexsbytez phase change material," in *2011 International Electron Devices Meeting*, (2011), pp. 3.4.1–3.4.4.
18. M. Stegmaier, C. Ríos, H. Bhaskaran, C. D. Wright, and W. H. Pernice, "Nonvolatile all-optical 1x2 switch for chip-scale photonic networks," *Adv. Opt. Mater.* **5**(1), 1600346 (2017).
19. F. De Leonardi, R. Soref, V. M. Passaro, Y. Zhang, and J. Hu, "Broadband electro-optical crossbar switches using low-loss ge 2 sb 2 se 4 te 1 phase change material," *J. Lightwave Technol.* **37**(13), 3183–3191 (2019).
20. J. Feldmann, N. Youngblood, X. Li, C. D. Wright, H. Bhaskaran, and W. H. Pernice, "Integrated 256 cell photonic phase-change memory with 512-bit capacity," *IEEE J. Sel. Top. Quantum Electron.* **26**(2), 1–7 (2020).
21. P. Xu, J. Zheng, J. K. Doylend, and A. Majumdar, "Low-loss and broadband nonvolatile phase-change directional coupler switches," *ACS Photonics* **6**(2), 553–557 (2019).
22. N. Farmakidis, N. Youngblood, X. Li, J. Tan, J. L. Swett, Z. Cheng, C. D. Wright, W. H. Pernice, and H. Bhaskaran, "Plasmonic nanogap enhanced phase-change devices with dual electrical-optical functionality," *Sci. Adv.* **5**(11), eaaw2687 (2019).
23. E. Gemo, S. G.-C. Carrillo, C. R. De Galarreta, A. Baldycheva, H. Hayat, N. Youngblood, H. Bhaskaran, W. H. Pernice, and C. D. Wright, "Plasmonically-enhanced all-optical integrated phase-change memory," *Opt. Express* **27**(17), 24724–24737 (2019).
24. Z. Cheng, C. Ríos, W. H. Pernice, C. D. Wright, and H. Bhaskaran, "On-chip photonic synapse," *Sci. Adv.* **3**(9), e1700160 (2017).
25. J. Feldmann, N. Youngblood, C. Wright, H. Bhaskaran, and W. Pernice, "All-optical spiking neurosynaptic networks with self-learning capabilities," *Nature* **569**(7755), 208–214 (2019).
26. J. Faneca, T. Domínguez Bucio, F. Y. Gardes, and A. Baldycheva, "O-band N-rich silicon nitride MZI based on GST," *Appl. Phys. Lett.* **116**(9), 093502 (2020).
27. Y. Tamura, H. Sakuma, K. Morita, M. Suzuki, Y. Yamamoto, K. Shimada, Y. Honma, K. Sohma, T. Fujii, and T. Hasegawa, "Lowest-ever 0.1419-dB/km loss optical fiber," in *Optical Fiber Communication Conference*, (Optical Society of America, 2017), pp. Th5D–1.
28. Y. Tamura, H. Sakuma, K. Morita, M. Suzuki, Y. Yamamoto, K. Shimada, Y. Honma, K. Sohma, T. Fujii, and T. Hasegawa, "The first 0.14-dB/km loss optical fiber and its impact on submarine transmission," *J. Lightwave Technol.* **36**(1), 44–49 (2018).
29. J. Tang, T. Hao, W. Li, D. Domenech, R. Baños, P. Muñoz, N. Zhu, J. Capmany, and M. Li, "Integrated optoelectronic oscillator," *Opt. Express* **26**(9), 12257–12265 (2018).
30. Y. Okawachi, K. Saha, J. S. Levy, Y. H. Wen, M. Lipson, and A. L. Gaeta, "Octave-spanning frequency comb generation in a silicon nitride chip," *Opt. Lett.* **36**(17), 3398–3400 (2011).
31. D. Pérez, I. Gasulla, L. Crudgington, D. J. Thomson, A. Z. Khokhar, K. Li, W. Cao, G. Z. Mashanovich, and J. Capmany, "Multipurpose silicon photonics signal processor core," *Nat. Commun.* **8**(1), 636 (2017).
32. J. Wang, H. Shen, L. Fan, R. Wu, B. Niu, L. T. Varghese, Y. Xuan, D. E. Leaird, X. Wang, F. Gan, W. Andrew M, and M. Qi, "Reconfigurable radio-frequency arbitrary waveforms synthesized in a silicon photonic chip," *Nat. Commun.* **6**(1), 5957 (2015).
33. H. Zhang, L. Zhou, B. M. A. Rahman, X. Wu, L. Lu, Y. Xu, J. Xu, J. Song, Z. Hu, L. Xu, and J. Chen, "Ultracompact si-gst hybrid waveguides for nonvolatile light wave manipulation," *IEEE Photonics J.* **10**(1), 1–10 (2018).
34. J. Zheng, A. Khanolkar, P. Xu, S. Colburn, S. Deshmukh, J. Myers, J. Frantz, E. Pop, J. Hendrickson, N. B. Doylend, and A. Majumdar, "Gst-on-silicon hybrid nanophotonic integrated circuits: a non-volatile quasi-continuously reprogrammable platform," *Opt. Mater. Express* **8**(6), 1551–1561 (2018).

35. X. Li, N. Youngblood, Z. Cheng, S. G.-C. Carrillo, E. Gemo, W. H. Pernice, C. D. Wright, and H. Bhaskaran, "Experimental investigation of silicon and silicon nitride platforms for phase-change photonic in-memory computing," *Optica* **7**(3), 218–225 (2020).
36. C. Rios, P. Hosseini, C. D. Wright, H. Bhaskaran, and W. H. Pernice, "On-chip photonic memory elements employing phase-change materials," *Adv. Mater.* **26**(9), 1372–1377 (2014).
37. X. Li, N. Youngblood, C. Ríos, Z. Cheng, C. D. Wright, W. H. Pernice, and H. Bhaskaran, "Fast and reliable storage using a 5 bit, nonvolatile photonic memory cell," *Optica* **6**(1), 1–6 (2019).
38. M. Rudé, J. Pello, R. E. Simpson, J. Osmond, G. Roelkens, J. J. van der Tol, and V. Pruneri, "Optical switching at $1.55\ \mu\text{m}$ in silicon racetrack resonators using phase change materials," *Appl. Phys. Lett.* **103**(14), 141119 (2013).
39. H. Liang, R. Soref, J. Mu, A. Majumdar, X. Li, and W. Huang, "Simulations of silicon-on-insulator channel-waveguide electrooptical 2×2 switches and 1×1 modulators using a $\text{Ge}_2\text{Sb}_2\text{Te}_5$ self-holding layer," *J. Lightwave Technol.* **33**(9), 1805–1813 (2015).
40. Y. Ikuma, Y. Shoji, M. Kuwahara, X. Wang, K. Kintaka, H. Kawashima, D. Tanaka, and H. Tsuda, "Small-sized optical gate switch using $\text{Ge}_2\text{Sb}_2\text{Te}_5$ phase-change material integrated with silicon waveguide," *Electron. Lett.* **46**(5), 368–369 (2010).
41. Y. Ikuma, T. Saiki, and H. Tsuda, "Proposal of a small self-holding 2×2 optical switch using phase-change material," *IEICE Electron. Express* **5**(12), 442–445 (2008).
42. M. Stegmaier, C. Ríos, H. Bhaskaran, and W. H. Pernice, "Thermo-optical effect in phase-change nanophotonics," *ACS Photonics* **3**(5), 828–835 (2016).
43. K. Kohary and C. D. Wright, "Electric field induced crystallization in phase-change materials for memory applications," *Appl. Phys. Lett.* **98**(22), 223102 (2011).
44. J. Zheng, S. Zhu, P. Xu, S. T. Dunham, and A. Majumdar, "Modeling electrical switching of nonvolatile phase-change integrated nanophotonic structures with graphene heaters," *ACS Appl. Mater. & Interfaces* (2020).